Chemical Engineering Science 199 (2019) 249–257

Contents lists available at ScienceDirect

Chemical Engineering Science

journal homepage: www.elsevier.com/locate/ces

# Continuum prediction of entrainment rates and agglomeration of gas-fluidized, lightly-cohesive particles

Kevin M. Kellogg, Peiyuan Liu, Christine M. Hrenya *

*University of Colorado at Boulder, Department of Chemical and Biological Engineering, United States*

## HIGHLIGHTS

- A novel continuum theory accurately predicts aggregation in a gas-solid flow.
- The continuum theory accurately predicts entrainment of cohesive particles.
- Aggregation leads to increased granular temperature and breakup of agglomerates.

## ARTICLE INFO

*Article history:*
Received 7 September 2018
Received in revised form 6 January 2019
Accepted 12 January 2019
Available online 23 January 2019

*Keywords:*
Cohesive particles
Agglomeration
Entrainment
Agglomerate breakage
Population balance

## ABSTRACT

In this work, a continuum theory for cohesive particles developed recently (Kellogg et al., 2017) is applied to lightly-cohesive particles in an unbounded, gas-solid riser. The novelty of this recent theory is its fundamental incorporation of the effects of the granular temperature (i.e., continuum measure of impact velocity) and the material and cohesion properties on the rates of aggregation and breakage of agglomerates. Here, we extend this theory to multiphase systems and place particular emphasis on its ability to predict entrainment rate, as past empirical correlations vary by orders of magnitude when applied to the same system (Chew et al., 2015). Specifically, continuum predictions of entrainment rates and agglomerate fraction are compared with Discrete Element Method (DEM) simulations of lightly-cohesive particles in a gas-solid flow. The agreement obtained for these quantities provides preliminary validation for the use of the continuum theory for cohesive particles in gas-solid flows.



## 1. Introduction

Much work has been done to predict the entrainment rate of particles from the risers of fluidized beds. Empirical correlations for the entrainment and transport disengagement height of particles in a fluidized bed give rise to predictions that vary many orders of magnitude when applied to the same system, even for non-cohesive particles (Cahyadi et al., 2015; Chew et al., 2015). Cohesive particles, which experience attraction from van der Waals forces, liquid bridging or other sources of cohesion, may stick together upon collision and form groups of particles called agglomerates (Castellanos, 2005). These agglomerates can decrease the entrainment of particles in a fluidized bed (Geldart et al., 1984) and further complicate the prediction of entrainment rates (Motlagh et al., 2014). A physically-based description of the entrainment and agglomeration of cohesive particles is needed for improved accuracy of predictions.

One approach to predicting the flows of cohesive particles is the Discrete Element Method (DEM). In DEM, each particle is tracked using Newton's second law, allowing for a direct incorporation of cohesive forces between particles (Mikami et al., 1998). Although DEM has been widely applied to flows of cohesive particles (e.g. (Anand et al., 2009; Chaudhuri et al., 2006; Figueroa et al., 2009; Galvin and Benyahia, 2014; Hou et al., 2012; Liu et al., 2016a, 2016b)), when compared to the continuum theory, DEM has a large computational overhead (van der Hoef et al., 2008). This computational overhead prevents DEM from being directly applied to predict the behavior of commercial-scale fluidized beds and risers, unlike continuum theory.

In recent work, we developed a continuum theory for rapid cohesive-particle flows based on first principles (Kellogg et al., 2017) – i.e., all inputs are physically based and no adjustable parameters are utilized. This continuum theory is composed of two coupled parts. The first part is a population balance, in which the number density of each agglomerate size is tracked, with changes arising from sink and source terms that represent the birth and death of an agglomerate size due to aggregation and breakage.

* Corresponding author.
*E-mail address:* hrenya@colorado.edu (C.M. Hrenya).

https://doi.org/10.1016/j.ces.2019.01.012
0009-2509/

The novel aspect of this continuum theory is that it utilizes fundamentally-based success factors of agglomeration and breakage (fractions of collisions that results in agglomeration and breakage) that depend on particle properties and the granular temperature, $T_s$, which is proportional to the variance of particle velocities from the local mean velocity ($T_s = m\langle(\mathbf{v}-\mathbf{u})^2\rangle/3$). Secondly, the new continuum theory for cohesive particles utilizes kinetic-theory-based closures for the transport coefficients in the granular momentum and energy balances. Specifically, the theory makes use of an effective coefficient of restitution (the ratio between post and pre-collisional impact velocities) in these closures to account for the additional collisional dissipation that cohesive particles experience relative to non-cohesive particles. This new continuum theory for cohesive particles was shown to perform well in a steady state, gravity-free, granular (no gas), simple shear flow and a granular homogeneous cooling system for lightly cohesive particles – i.e., mostly singlets (primary particles) and doublets (two-particle agglomerates).

In the current work, the continuum theory for cohesive particles that was previously developed for granular systems (Kellogg et al., 2017) is extended to gas-solids systems and then applied to an unbounded riser with lightly-cohesive particles. In this riser, gravity exerts a downward force on the particles and an upward gas flow exerts an upward drag force on the particles. Particular emphasis is placed on the ability of the new theory to predict entrainment rates given the orders-of-magnitude variations observed between previous correlations (Chew et al., 2015). This ability of the extended theory is tested via direct comparison with DEM simulations of the same unbounded riser.

## 2. Methods

### 2.1. Continuum

While the continuum theory for cohesive particles is generally applicable to various material properties, sources of cohesion, and systems, the particles considered here are lightly-cohesive. Generally, the particles only present themselves as singlets (primary particles) and doublets (two-particle agglomerates, so only singlets and doublets are considered here). The resulting population balance equations are (Kellogg et al., 2017)

$$\frac{\partial n_1}{\partial t} + \nabla\cdot(\mathbf{u}_1 n_1) = -2N_{1,1}S_{agg,1,1} + 2N_{1,2}S_{break,1,2} \tag{1}$$

$$\frac{\partial n_2}{\partial t} + \nabla\cdot(\mathbf{u}_2 n_2) = N_{1,1}S_{agg,1,1} - N_{1,2}S_{break,1,2} \tag{2}$$

where $n_1$ and $n_2$ are the number density of singlets and doublets, respectively, and $\mathbf{u}$ is the velocity of the respective agglomerate size. $N_{1,1}$ and $N_{1,2}$ are the collision frequencies of singlets with other singlets and doublets, respectively. $S_{agg,1,1}$ is the success factor of agglomeration for singlet-singlet collisions (the fraction of collisions that result in agglomeration), and $S_{break,1,2}$ is the success factor of breakage of singlet-doublet collisions (the fraction of collisions that result in breakage). The closures for the success factors and collision frequencies are summarized in Table 1 (Kellogg et al., 2017). The term $-2N_{1,1}S_{agg,1,1}$ in Eq. (1) is the death rate of singlets due to agglomeration, and the term $N_{1,2}S_{break,1,2}$ in Eq. (1) is the birth rate of singlets from the breakage of doublets due to collisions with singlets. The term $N_{1,1}S_{agg,1,1}$ in Eq. (2) represents the birth rate of doublets from agglomeration of singlets and the term $-N_{1,2}S_{break,1,2}$ in Eq. (2) represents the death rate of doublets due to collisions with singlets. The rate of breakage of doublets from collisions with other doublets is neglected due to the lightly-cohesive assumption – i.e., such collisions are infrequent relative to singlet-singlet and singlet-doublet collisions.

To calculate the success factors of agglomeration and breakage in Table 1, particle- and cohesion-specific inputs are required. First, a critical velocity of agglomeration $v_{a,crit}$ is needed, which corresponds to the velocity below which all collisions result in agglomeration. The critical velocity of agglomeration was varied in this work to explore particles subject to different amounts of cohesion. Additionally, a critical velocity of breakage $v_{b,crit}$, which represents the velocity above which collisions with agglomerates will result in breakage of the agglomerate is needed. Finally, a collision cylinder diameter $d_{1,2}$, which gives the sweep area of a pair of colliding agglomerates/primary particles and is used to calculate the collision frequency, is required. These physical inputs ($v_{a,crit}$, $v_{b,crit}$, and $d_{1,2}$) were determined in previous work from simple shear flow simulations of 64 μm diameter glass beads undergoing van der Waals cohesion and are listed in Table 2 (Kellogg et al., 2017). The van der Waals cohesion model used in said DEM simulations is described below in Eqs. (34) and (35). Simple shear flow simulations were used since the inputs (critical velocities and collision diameter) are sensitive to collision orientation, and the distribution

**Table 2**
Continuum theory inputs determined from DEM (Kellogg et al., 2017).

| Parameter | Value |
|---|---|
| Non-dimensionalized critical velocity of breakage | $v_{b,crit,1,2}/v_{a,crit,1,1} = 1.502$ |
| Non-dimensionalized collision cylinder diameter | $d_{1,2}/d_1 = 1.2155$ |

**Table 1**
Auxiliary equations for continuum theory (Kellogg et al., 2017).

$$S_{agg,1,1} = 1 - \exp\left[\frac{-v_{a,crit,1,1}^2}{2T_s\left[\frac{6}{m_1 dof_1}\right]}\right] \tag{3}$$

$$S_{break,1,1} = \exp\left[\frac{-v_{b,crit,1,2}^2}{2T_s\left[\frac{3}{m_1 dof_1}+\frac{3}{m_2 dof_2}\right]}\right] \tag{4}$$

$$N_{1,1} = n_1 n_1 \pi d_1^3 g_0 \left[\frac{4}{d_1}\left(\frac{T_s}{\pi\frac{6}{m_1 dof_1}}\right)^{1/2}\right] \tag{5}$$

$$N_{1,2} = n_1 n_2 \pi d_{1,2}^3 g_0 \left[\frac{4}{d_{1,2}}\left(\frac{T_s}{\pi\left[\frac{3}{m_1 dof_1}+\frac{3}{m_2 dof_2}\right]}\right)^{1/2}\right] \tag{6}$$

$$e_{eff}(v_n) = H(v_n - v_{a,crit,1,1})\left(e_{int}^2 + \frac{(e_{int}^2-1)D_{well}}{4m_1 v_n^2}\right)^{1/2} \tag{7}$$

$$f(v_n) = \frac{v_n}{T_s\left[\frac{6}{m_1 dof_1}\right]}\exp\left[\frac{-v_n^2}{2T_s\left[\frac{6}{m_1 dof_1}\right]}\right] \tag{8}$$

$$\langle e_{eff}\rangle = \frac{\int_{v_{a,crit,1,1}}^{\infty} e_{eff}(v_n)f(v_n)dv_n}{\int_{v_{a,crit,1,1}}^{\infty} f(v_n)dv_n} \tag{9}$$

$$m_2 = 2m_1 \tag{10}$$

$$m_1 = \frac{\rho d_1^3}{6} \tag{11}$$

$$dof_1 = 3 \tag{12}$$

$$dof_2 = 5 \tag{13}$$

$$g_0 = \frac{1-\varepsilon_s/2}{(1-\varepsilon_s)^3} \tag{14}$$

$$D_{well} = \frac{4m_1 v_{a,crit,1,1}^2 e_{int}^2}{1-e_{int}^2} \tag{15}$$

$$H(x) = \begin{cases} 0 & x \leqslant 0 \\ 1 & x > 0 \end{cases} \tag{16}$$

of impact orientations in simple shear flow is similar to that observed in the unbounded riser flow (Kellogg et al., 2017; Liu et al., 2017).

Note that although the population balances solved in the current work are identical to those considered in previous work (Kellogg et al., 2017), a momentum balance is solved for each agglomerate size in the current work, whereas a single momentum balance was considered in previous work. This new aspect traces to the extension of the cohesive continuum theory to a gas-solid flow. More specifically, the presence of the gas phase necessitates a gas-solid drag term in the solids-phase momentum balance. Since different agglomerate sizes experience different amounts of drag and consequently have different slip velocities (difference of velocity between an agglomerate size and the gas), a separate momentum balance needs to be solved for each agglomerate size. Additionally, the difference in relative velocities between the agglomerate sizes leads to terms associated with solids-solids drag, which also was not present in previous systems explored (simple shear flow and homogeneous cooling of granular materials). The closures for the momentum balances used here were derived for non-cohesive spheres of different sizes (polydispersity), but are being applied now to cohesive, non-spherical agglomerates as a first approximation. The effect of cohesion causing additional dissipation during collisions is captured in these momentum balance closures used here by utilizing the effective coefficient of restitution $\langle e_{eff}\rangle$ in the calculation of these closures. The effect of the non-spherical nature of agglomerates is not accounted for in the momentum balance closures originally derived for non-cohesive spheres. No kinetic-theory-based closures account for non-spherical particles, however, so this approximation is necessary. The momentum balances are (Iddir and Arastoopour, 2005)

$$\frac{\partial(m_1 n_1 \mathbf{u}_1)}{\partial t} + \nabla\cdot(m_1 n_1 \mathbf{u}_1\mathbf{u}_1) = -\nabla\cdot(P\mathbf{I}+\tau) + m_1 n_1 \mathbf{g} - \varepsilon_1 \Delta P_g/H\hat{\mathbf{j}} + 2\mathbf{u}_2 N_{1,2} S_{break,1,2} - 2\mathbf{u}_1 N_{1,1} S_{agg,1,1} + \mathbf{F}_{\mathbf{drag},\mathbf{g},1} + \mathbf{F}_{\mathbf{drag},2,1} \tag{17}$$

$$\frac{\partial(m_2 n_2 \mathbf{u}_2)}{\partial t} + \nabla\cdot(m_2 n_2 \mathbf{u}_2\mathbf{u}_2) = -\nabla\cdot(P\mathbf{I}+\tau) + m_2 n_2 \mathbf{g} - \varepsilon_2 \Delta P_g/H\hat{\mathbf{j}} - 2\mathbf{u}_2 N_{1,2} S_{break,1,2} + 2\mathbf{u}_1 N_{1,1} S_{agg,1,1} + \mathbf{F}_{\mathbf{drag},\mathbf{g},2} - \mathbf{F}_{\mathbf{drag},2,1} \tag{18}$$

where $P$ is the granular pressure, $\mathbf{I}$ is the identity matrix, and $\boldsymbol{\tau}$ is the solids-phase stress. The single granular temperature $T_s$ was used as the granular temperature of the singlets $T_1$ and the granular temperature of the doublets $T_2$ in the closures for the solids stress and pressure from Iddir and Arastoopour (2005). In Eqs. (17) and (18), the first term on the left side is the transient term, and the second term on the left side is the convective term. On the right side of these equations, the first term is the divergence of stresses (diffusion), the second term represents gravitational forces, the third term incorporates the gas-phase pressure drop induced on the system, the fourth term is the gas-solid drag force, the fifth term is the (solids-solids) drag force due to collisions between singlets and doublets, the sixth term is the exchange of momentum due to breakage, and the last term is the exchange of momentum due to aggregation. Since few doublets were observed in the system, constitutive relations for these terms were approximated using closures derived from monodisperse kinetic theory (Garzó and Dufty, 1999) using the total (local) solids volume fraction, singlet diameter and the effective coefficient of restitution (as detailed below). $\mathbf{g}$ is the gravitational vector, which takes a value of $-9.81$ m/s$^2$ in the $y$-direction (upward). The term $\Delta P_g/H$ was used to set the gas-phase pressure drop across the system, which was equal to the weight of the system divided by the density (i.e. $\Delta P_g/H = n_1 m_1 + n_2 m_2 + \rho_g \varepsilon_g$ where $\varepsilon_g$ is the gas volume fraction). The terms $2\mathbf{u_1} N_{1,1} S_{agg,1,1}$ and $2\mathbf{u_2} N_{1,2} S_{break,1,2}$ represent the transfer of momentum from one agglomerate size to another during aggregation and breakage, respectively. The term $\mathbf{F}_{\mathbf{drag},\mathbf{g},\mathbf{i}}$ represents gas-solid drag, and is given by:

$$\mathbf{F}_{\mathbf{drag},\mathbf{g},\mathbf{i}} = K_{g,i}(\mathbf{u_g} - \mathbf{u_i}) \tag{19}$$

where $K_{g,i}$ is the drag coefficient given by an extension (Benyahia et al., 2006) of that originally proposed by Koch, Hill, and Ladd (Hill et al., 2001) with the total solid volume fraction used for the solid volume fraction. The volume equivalent diameter (the diameter of a sphere with an equivalent volume as the agglomerate) of each agglomerate size is used for the diameter. These closures are summarized in Appendix A. The solids drag represents momentum transfer between agglomerate sizes due to collisions of agglomerates of different sizes. These closures were derived for spheres of different sizes, but are used here for non-spherical agglomerates (assumed to be spherical) of different sizes. The closures are given by (Iddir and Arastoopour, 2005):

$$\mathbf{F}_{\mathbf{drag},2,1} = K_{2,1}(\mathbf{u}_2 - \mathbf{u}_1) \tag{20}$$

where

$$K_{2,1} = \frac{d_{1,2}}{4}\frac{m_1 m_2}{m_1+m_2} g_0 (1 + \langle e_{eff}\rangle) n_1 n_2 \left(\frac{m_1}{T_s}\right)^3 R_2 \sqrt{\pi} \tag{21}$$

$$R_2 = \frac{1}{2A_{12}D_{12}^2} \tag{22}$$

$$A_{12} = \frac{m_1+m_2}{2T_s}, \text{and} \tag{23}$$

$$D_{12} = \frac{m_1 m_2}{2(m_1+m_2)T_s} \tag{24}$$

where $g_0$ is the radial distribution function given in Eq. (14) (Mansoori, 1971) and $T_s$ is the granular temperature. Eqs. (20)–(24) were derived for non-cohesive spheres, but are being applied here to agglomerates.

In order to solve for the granular temperature $T_s$ appearing in the closures for the population and momentum balances, a granular energy balance is solved. Granular energy refers to the random, fluctuating kinetic energy associated with particle motion varying from the mean motion. Here, since most of the particles are in singlets, a single granular energy balance is solved for granular temperature $T_s$ (Iddir and Arastoopour, 2005; Kellogg et al., 2017)

$$\frac{\partial\left(\frac{3}{2}nT_s\right)}{\partial t} + \nabla\cdot\left(\frac{3}{2}nT_s\mathbf{u}_1\right) = -(P\mathbf{I}+\tau):\nabla\mathbf{u}_1 - \nabla\cdot\mathbf{q} - \zeta T_s + (\mathbf{u}_1 - \mathbf{u}_2)\cdot\mathbf{F}_{\mathbf{drag},2,1} \tag{25}$$

where $n$ is the total number density and closures for $\mathbf{q}$ and $\zeta$ come from a monodisperse kinetic theory using the effective coefficient of restitution $\langle e_{eff}\rangle$ (Eq. (9)), total solid volume fraction, and singlet diameter (Garzó and Dufty, 1999; Kellogg et al., 2017). The first term on the left side of Eq. (25) is represents the change of granular energy with time, and the second term represents the convection of granular energy. The first term on the right side of the equation is the generation of granular energy due to shear, the second term is the diffusion of granular energy, the third term is the dissipation of granular energy due to inelastic collisions. The final term in Eq. (25) is the generation of granular energy due to differences in relative velocity between the different agglomerate sizes. This final term was not included in previous work (Kellogg et al., 2017) since the singlets and doublets all travelled with the same velocity. The gas phase included in the current work leads to different agglomerate sizes having different drag and thus a nonzero relative velocity between them, necessitating the final term in Eq. (25). Realistically, the granular temperature of the singlets $T_1$ and the doublets $T_2$ will

be unequal. Again, since the majority of the particles are in singlets, a single granular temperature $T_s$ which will be closer to the singlet granular temperature is considered. The main potential ramification of this assumption is that the singlet-doublet success factor of breakage, as well as the singlet-doublet collision frequency, which are dependent on the granular temperature of the doublet, may be slightly inaccurate. These two terms appear in the population balance in the rate of breakage of doublets terms.

Finally, for the gas phase, the governing mass and momentum balances are (Gidaspow, 1994)

$$\frac{\partial\left(\rho_g\varepsilon_g\right)}{\partial t}+\nabla\cdot\left(\rho_g\varepsilon_g\mathbf{u_g}\right)=0 \tag{26}$$

$$\frac{\partial\left(\rho_g\varepsilon_g\mathbf{u_g}\right)}{\partial t}+\nabla\cdot\left(\rho_g\varepsilon_g\mathbf{u_g}\mathbf{u_g}\right)=-\nabla\cdot\left(P_g\mathbf{I}+\mu\nabla\mathbf{u_g}\right)+\varepsilon_g\Delta P_g/H\hat{\mathbf{j}}-\varepsilon_g\rho_g\mathbf{g}-\mathbf{F_{drag,g,1}}-\mathbf{F_{drag,g,2}} \tag{27}$$

In Eqs. (26) and (27), the left side represents acceleration. In Eq. (27), on the right side, the first term is the divergence of the stress tensor and gives diffusion of momentum, the second term institutes the pressure drop, the third term represents gravity, and the last two terms represent the drag force exerted on the singlets and doublets respectively.

### 2.2. DEM

For DEM, the position **x** and velocity **v** of each particle are updated according to Newton's second law of motion, using Euler integration. The forces acting on the particles are given by

$$\mathbf{F}=m\frac{d\mathbf{v}}{dt}=\mathbf{F_{cont}}+\mathbf{F_{coh}}+\mathbf{F_{drag}}+\mathbf{F_g} \tag{28}$$

where **F** is the total force, $\mathbf{F_{coh}}$ is the cohesive force, $\mathbf{F_{cont}}$ is the contact force, $\mathbf{F_{drag}}$ is the drag force and $\mathbf{F_g}$ is the gravitational force acting on a given particle. The Hertzian contact expression was used to give the magnitude of the contact force:

$$F_{cont}=\begin{cases}\frac{4E_{eff}\sqrt{R_{eff}}}{3}\delta^{3/2}+\eta\frac{d\delta}{dt} & \delta\geqslant 0\\ 0 & \delta<0\end{cases} \tag{29}$$

where

$$E_{eff}=\frac{E_iE_j}{E_i\left(1+\nu_j^2\right)+E_j\left(1+\nu_i^2\right)} \tag{30}$$

$$R_{eff}=\frac{R_iR_j}{R_i+R_j} \tag{31}$$

$$\eta=\frac{-2\sqrt{15m_{eff}E_{eff}}R_{eff}^{\frac{1}{4}}\ln(e_{int})}{3\sqrt{\pi^2+\ln^2(e_{int})}}\delta^{1/4} \tag{32}$$

$$m_{eff}=\frac{m_im_j}{m_i+m_j} \tag{33}$$

and $\delta$ is the overlap of contacting particles, $E$ is the Young's modulus, $\nu$ is the Poisson ratio, $R$ is the particle radius, $e_{int}$ is the intrinsic coefficient of restitution, and $m$ is the particle mass. The drag force was calculated using an extension (Benyahia et al., 2006) of the Koch-Hill-Ladd (Hill et al., 2001) drag law using the primary particle diameter and the local solid volume fraction, as given in Eq. (19) above. Finally, the cohesion was calculated using the Rabinovich expression for cohesive force (Rabinovich et al., 2000) extended for interactions between two particle surfaces that each have two scales of roughness (Liu et al., 2016b)

$$F_{coh}(D>D_{min})=\frac{A}{6}\left[\frac{R_iR_j}{(R_i+R_j)\left(D+y_{iL}+y_{jL}+y_{iS}+y_{jS}\right)^2}+\frac{R_ir_{jL}}{(R_i+r_{jL})\left(D+y_{iL}+y_{iS}+y_{jS}\right)^2}\right. \tag{34}$$

$$+\frac{R_ir_{jS}}{(R_i+r_{jS})\left(D+y_{iL}+y_{iS}\right)^2}+\frac{r_{iL}R_i}{(r_{iL}+R_j)\left(D+y_{iS}+y_{jL}+y_{jS}\right)^2}$$

$$+\frac{r_{iL}r_{jL}}{(r_{iL}+r_{jL})\left(D+y_{iS}+y_{jS}\right)^2}+\frac{r_{iL}r_{jS}}{(r_{iL}+r_{jS})\left(D+y_{iS}\right)^2}$$

$$\left.+\frac{r_{iS}R_j}{(r_{iS}+R_j)\left(D+y_{iL}+y_{jS}\right)^2}+\frac{r_{iS}r_{jL}}{(r_{iL}+r_{jL})\left(D+y_{jS}\right)^2}+\frac{r_{iS}r_{jS}}{(r_{iS}+r_{jS})D^2}\right]$$

where

$$r_{kl}=\frac{\lambda_{kl}^2}{32k_1rms_{kl}},\ y_{kl}=k_1rms_{kl}$$

and $\lambda$ is the wavelength of the roughness, $k_1$ = 1.817 is a geometric constant, $rms_{kl}$ is the root mean square height of asperities, $r_{kl}$ is the radius of asperities, and $y_{kl}$ is the asperity height, with subscript $k$ taking values of $i$ or $j$ for different particles, and subscript $l$ taking values of $S$ or $L$ for small or large scale asperities. $A$ is the Hamaker constant, $R$ is the particle radius, $D$ is the separation distance between the highest asperity of the two particles, and $D_{min}$ is the cut-off distance, frequently taken to be the intermolecular separation distance. The cut-off distance represents the separation between surfaces at which the cohesive force is capped in order to prevent an infinite cohesive force for $D$ = 0. In other words, when particles are separated by less than the minimum cut off distance,

$$F_{coh}(D\leqslant D_{min})=F_{coh}(D_{min}) \tag{35}$$

The particle properties used in this study are summarized in Table 3. The Poisson ratio, primary particle diameter, particle density, coefficient of restitution, and small and large scale roughness and wavelengths are characteristic of silica glass particles. The Young's modulus chosen here is significantly smaller than the literature value for glass and was chosen to enhance computational efficiency (Liu et al., 2016c). The gas properties are characteristic of air. The system size was chosen so that the DEM simulations would have on the order of 10,000 particles so the system was small enough to minimize hydrodynamic instabilities (clustering) but large enough to ensure good statistics.

In the DEM simulation, the gas phase continuity equation was identical to Eq. (26) used in the continuum simulations. The

**Table 3**
Particle, gas, and system properties used in simulations.

| Property | Symbol | Value | Units |
|---|---|---|---|
| Young's modulus | $E$ | 10 | MPa |
| Poisson ratio | $\nu$ | 0.3 | – |
| Diameter | $d$ | 64 | μm |
| Particle density | $\rho_s$ | 2500 | kg/m$^3$ |
| Intrinsic coefficient of restitution | $e_{int}$ | 0.97 | – |
| Large scale wavelength | $\lambda_L$ | 2671 | nm |
| Small scale wavelength | $\lambda_S$ | 369 | nm |
| Large scale roughness | $rms_L$ | 22.17 | nm |
| Small scale roughness | $rms_S$ | 2.411 | nm |
| Gas viscosity | $\mu$ | $1.8335\cdot10^{-5}$ | Pa•s |
| Gas density | $\rho_g$ | 0.97 | kg/m$^3$ |
| Target gas velocity | $u_{g,y}$ | 0.515 | m/s |
| System width and depth | $W=L$ | 0.3234375 | cm |
| System height | $H$ | 1.4375 | cm |
| Grid size | $\Delta x/d$ | 2 | – |

momentum balance used was similar to the Eq. (27) used in the continuum simulations, except without the term $\Delta P_g/H$.

### 2.3. Unbounded riser system

A schematic of the unbounded riser geometry is shown in Fig. 1, with dimensions summarized in Table 3. All side walls were periodic for both the gas and solid phases in both the DEM and continuum simulations. The DEM simulations were performed using the MFiX 2016-1 multiphase computational fluid dynamics package (Syamlal et al., 1993). In the DEM simulations, the top and bottom boundaries were periodic for the solids phase. The pressure at the bottom boundary for the gas phase was adjusted dynamically to achieve the desired gas flow rate summarized in Table 3. The top boundary of the DEM simulations for the gas phase was a pressure outlet. The continuum simulations were carried out independently from the DEM simulations using ANSYS Fluent 17.0. In the continuum simulations, periodic boundary conditions were used for both the gas and solids phases on the top and bottom boundaries with a pressure gradient applied throughout the system in the upwards $y$-direction. This pressure gradient was equal to the weight of the system divided by the cross-sectional area, such that the system did not accelerate. Since fully periodic boundary conditions were used in the continuum theory, the system can be viewed as a moving reference frame. In order to compare the results from a moving reference (continuum theory) directly with that of the fixed reference frame (DEM), the continuum velocities for the gas, singlets, and doublets were all adjusted by the same amount such that the DEM and continuum gas velocities were equal.

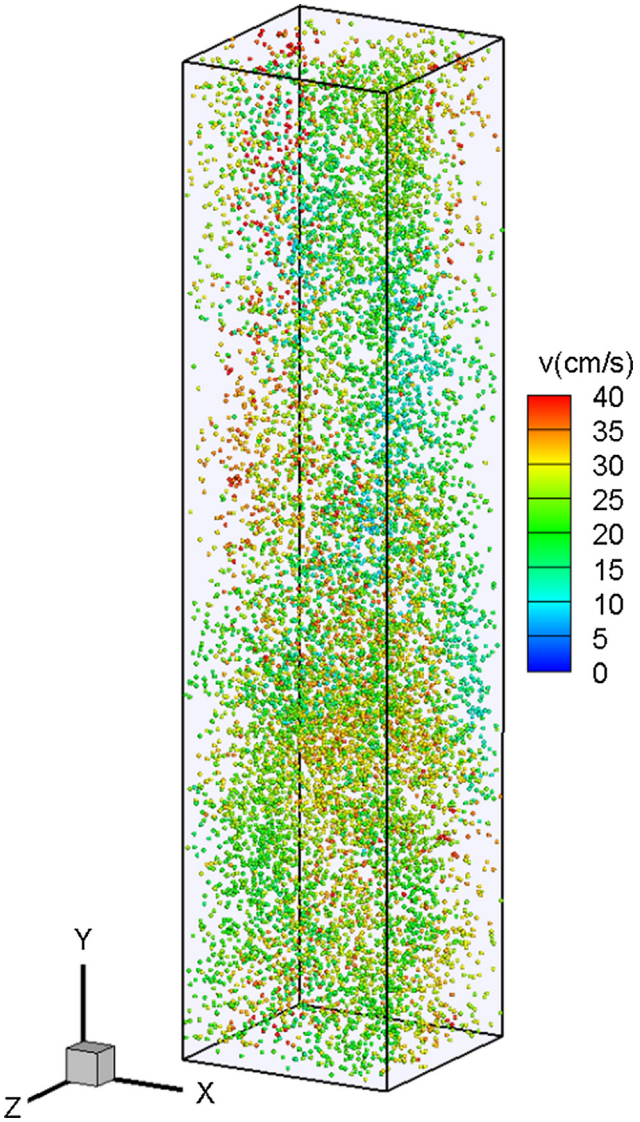


**Fig. 1.** Schematic of riser flow used in DEM simulations.

Both the DEM and continuum simulations were initialized with no particles in agglomerates, and with zero mean velocity for the gas and solids. The initial positions of the DEM particles were random, while the continuum solid volume fraction was uniform. The solid volume fraction used in the continuum predictions was arbitrary, and the corresponding number of particles were modeled in the DEM simulations. The initial granular temperature of the continuum predictions was set to $T_s/m_1 = 10^{-6}\,\mathrm{m^2/s^2}$. Simulations were run for 2 s, as the gas and solid velocities and agglomerate fractions were found to reach steady state after 1 s. Unless noted otherwise, the error bars on DEM results show the standard deviation over the last second of simulation time when the system was at steady state. The continuum results lack error bars as they show the final steady-state solution, which does not vary.

In Case I, the solid volume fraction was fixed at $\varepsilon_s = 0.01$ and the Hamaker constant $A$ was changed to change the cohesive force (Eq. (34)) between particles. Changing the Hamaker constant changed the critical velocity of agglomeration $v_{a,crit,1,1}$ (which took values of 0.22–0.59 cm/s). The critical velocity of agglomeration was determined by performing DEM simulations of two particle collisions. In Case II, the critical velocity of agglomeration was fixed at 0.34 and 0.59 cm/s, and the solid volume fraction was varied from $\varepsilon_s = 0.0025$ to 0.04. These same conditions were used in both the DEM simulations and continuum theory predictions.

## 3. Results and discussion

For Case I where the level of cohesion (i.e., critical velocity of agglomeration) is varied, the DEM results and continuum predictions for the fraction of particles in agglomerates, and the entrainment rate are shown in Fig. 2a and b respectively. The fractions of particles in each agglomerate size observed in DEM are shown in Fig. 2c. First, we consider the fraction of particle in agglomerates (Fig. 2a). Qualitatively, both the DEM simulations and continuum predictions indicate that as the critical velocity of agglomeration (cohesion level) increases, the fraction of particles in agglomerates increases. Namely, as the particles are made more cohesive, collisions are more likely to result in aggregation and less likely to result in breakage, therefore a higher fraction of particles agglomerate.

From a quantitative standpoint, the continuum theory underpredicts the agglomerate fraction by up to 45% over the critical velocities studied. One source of error is that the DEM simulations allow agglomerates larger than doublets to form, whereas the continuum theory as applied here incorporates only singlets and doublets. Specifically, larger agglomerates than doublets are forming in the DEM simulations at higher critical velocities, but not at lower critical velocities, as seen in Fig. 2c. This increase in larger agglomerates corresponds to the increasing deviation in fraction of particles in agglomerates observed between DEM and the continuum theory in Fig. 2a, suggesting that the presence of agglomerates larger than doublets contribute to the deviation.

Next, we consider the entrainment rate. Qualitatively, as the critical velocity of aggregation (cohesion level) increases, the entrainment rate remains relatively constant for DEM and decreases slightly for the continuum theory. In the continuum theory, an agglomerate is treated as a single spherical particle with an effective diameter larger than the primary particle diameter. This

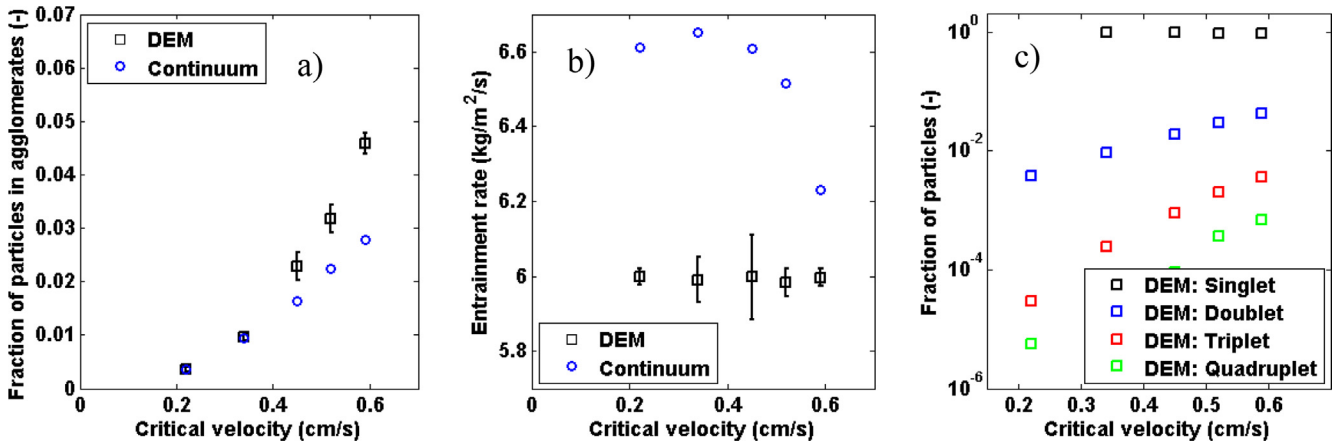


**Fig. 2.** Case I: constant volume fraction 0.01 and varying critical velocities. (a) Agglomerate fraction observed in DEM and continuum predictions, (b) entrainment rate observed in DEM and continuum predictions, and (c) fraction of particles in various agglomerate sizes observed in DEM. Error bars show 95% confidence interval of five DEM repeats.

effective diameter leads to a larger drag (equation for $K_g$ in Appendix A) than would be exerted on a primary particle, but less than the drag on two primary particles. Therefore, when particles agglomerate, they experience a net decrease in drag, an increase in terminal velocity and hence a decrease in entrainment rate. In DEM simulations, however, the diameter of particles in agglomerates is not changed in the drag law, but the presence of agglomerates is instead accounted for by the increase in the local solid volume fraction. The effective particle diameter has a greater effect on the drag reduction of agglomerates than the local solid volume fraction (equation for $K_g$ in Appendix A), which explains why the DEM entrainment rate remains relatively constant while the continuum theory exhibits a decrease in entrainment rate. A brief exploration was performed to determine the entrainment rate predicted by the continuum theory when the effective diameter of agglomerates was set equal to that of singlets. The results of this exploration (not shown) indicated that the continuum theory under-predicted the DEM entrainment rate by 3–7%, a marginal improvement to the over-prediction shown in Fig. 2b.

From a quantitative standpoint, the continuum theory over-predicts the DEM entrainment rate by less than 15% over the range of critical velocities studied here. Note that previous predictions of entrainment rates from empirical correlations vary by orders of magnitude (Chew et al., 2015). The relatively good quantitative agreement of agglomerate fraction and entrainment rate between the continuum theory and DEM simulations observed here provides preliminary support for the validity of using an extension of the recent continuum theory for cohesive particles (Kellogg et al., 2017) applied to gas-solid flow.

Next, we consider the impact of changing the solids concentration while maintaining a constant level of cohesion, as shown in Fig. 3. The fraction of particles in agglomerates is given in Fig. 3a and c for different levels of cohesion. A non-monotonic trend of agglomerate fraction with increasing solid volume fraction occurs. Two competing mechanisms lead to this behavior, as detailed below.

First, the increasing solid volume fraction directly affects agglomeration and breakage by increasing the collision frequencies $N_{1,1}$ and $N_{1,2}$ (Eqs. (5) and (6)) in Eqs. (1) and (2). This increase of collision frequency leads to an increase in aggregation and an increase in breakage (terms on right side of Eqs. (1) and (2)). The increase in agglomeration is greater than the increase in breakage since it becomes increasingly difficult to break up agglomerates as they grow in size since larger agglomerates can undergo internal dissipation and rearranging without breakage (Ringl et al., 2012). This increase in agglomeration relative to breakage leads to an increase the fraction of particles in agglomerates.

Second, the increasing solid volume fraction indirectly affects agglomeration and breakage by affecting the granular temperature. As solids volume fraction increases, the collision frequency increases and an increase in generation of granular energy from collisional generation between primary particles and doublets (the $(\mathbf{u_1} - \mathbf{u_2})\cdot\mathbf{F_{drag,2,1}}$ term in Eq. (25)) results. Namely, because agglomerates have a higher slip velocity (relative velocity between solid and gas phases) compared to primary particles, the primary particles move upwards faster than agglomerates. The resulting collisions increase with solid volume fraction, thereby leading to a monotonically increasing granular temperature for DEM simulations and an increasing temperature for solid volume fractions of $\varepsilon_s > 0.005$ for the continuum theory (see Fig. 4). Although the increased granular temperature further increases the collision frequencies $N_{1,1}$ and $N_{1,2}$ (Eqs. (5) and (6)), it also decreases the success factor of aggregation $S_{agg,1,1}$ and increases the success factor of breakage $S_{break,1,2}$ (Eqs. (3) and (4)) in Eqs. (1) and (2) (i.e. higher impact velocities, or granular temperature, decrease the likelihood of aggregation and increase the likelihood of breakage, leading to a smaller fraction of particles of particles in agglomerates). This behavior is dominant on the left of the minimum ($\varepsilon_s = 0.01$) in plots 3a and 3c in DEM. Exceptions only occur in the continuum prediction at the two lowest solid volume fractions in Fig. 3a and c, where instabilities cause a different behavior, as discussed below. For the remaining systems explored, which are all stable, the continuum theory under-predicts the agglomerate fraction by less than 75%.

Evidence for the instabilities predicted by the continuum theory at low solid concentrations and a critical velocity of 0.34 cm/s is shown in Fig. 4b and c. Namely, instabilities are not observed at higher solid volume fractions (Fig. 4b), but are seen at lower solid volume fractions (Fig. 4c). Similar unstable behavior is observed for a critical velocity of 0.59 cm/s (figure not shown for the sake of brevity), though the instabilities and corresponding increase in granular temperature are less pronounced. These instabilities are not present in any of the DEM simulations. The instabilities observed in the continuum simulations generate local gradients of solid velocity and thus increase shear, thereby leading to an increased generation of granular energy. This high granular energy corresponds to higher impact velocities upon collision, and hence the low agglomerate fractions at the two lowest solid volume fractions in Fig. 3c. At higher solid volume fractions ($\varepsilon_s > 0.005$), no instabilities exist, so the granular temperature is not inflated by this mechanism.

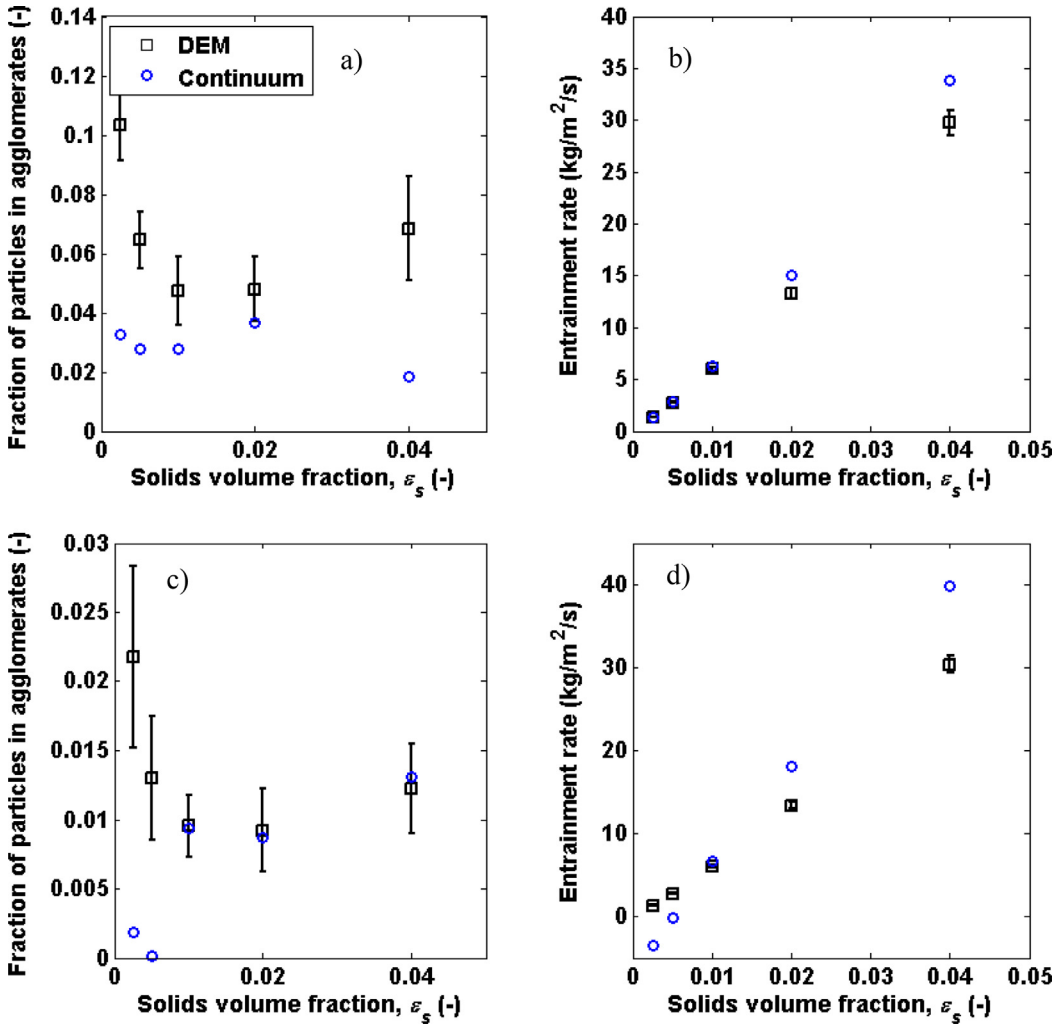


**Fig. 3.** Case II: constant critical velocities and varying solid volume fractions. (a) Agglomerate fraction when $v_{a,crit}$ = 0.59 cm/s, (b) entrainment rate when $v_{a,crit}$ = 0.59 cm/s, (c) agglomerate fraction when $v_{a,crit}$ = 0.34 cm/s, and (d) entrainment rate when $v_{a,crit}$ = 0.34 cm/s.

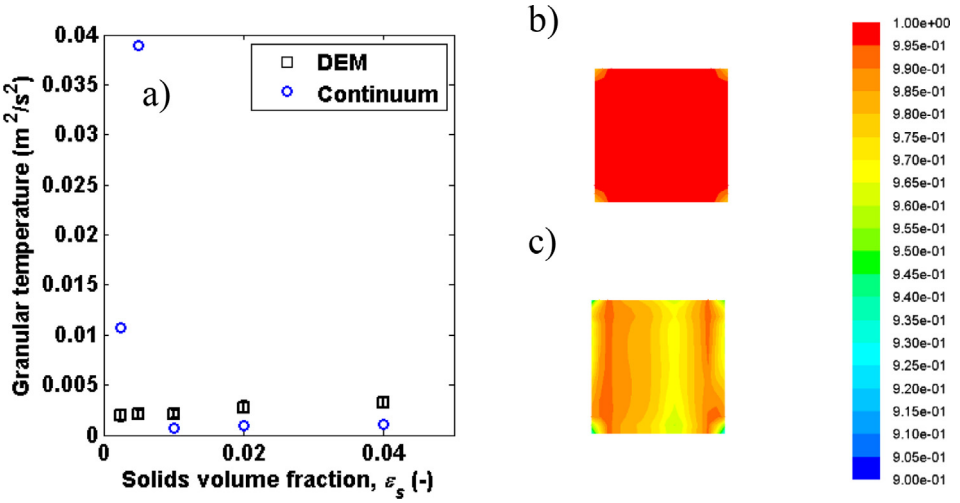


**Fig. 4.** (a) Granular temperature observed in DEM and continuum when $v_{crit}$ = 0.34 cm/s, (b) snapshot of gas volume fraction viewed from above ($y$ = 1.4375 cm) for (stable) case where $\varepsilon_s$ = 0.02 and $v_{a,crit}$ = 0.34 cm/s, (c) snapshot of gas volume fraction profile for (unstable) case where $\varepsilon_s$ = 0.00225 and $v_{a,crit}$ = 0.34 cm/s.

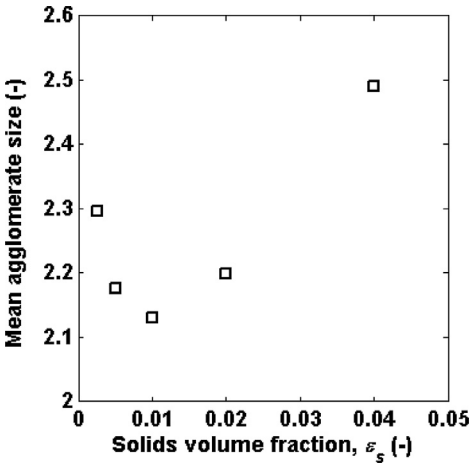


**Fig. 5.** Mean agglomerate size observed in DEM when $v_{a,crit}$ = 0.59 cm/s.

Next, we consider the entrainment rate. Fig. 3b and d show the entrainment rate increasing with solid volume fraction. This behavior is expected since entrainment rate is directly proportional to the solid volume fraction (i.e. entrainment rate $J_s = \rho_s \varepsilon_s \mathbf{u_s}$). Moreover, as solid volume fraction is increased, $\mathbf{u_s}$ increases slightly as well due to increasing drag and decreased terminal (slip) velocity at higher solid volume fractions. These two effects both lead to an increase in entrainment rate, though the latter dependence of $\mathbf{u_s}$ on $\varepsilon_s$ is weak compared to the direct proportionality between $J_s$ and $\varepsilon_s$. Quantitatively, the entrainment rate predicted by the continuum theory is in good agreement with that observed in the DEM simulations. For stable systems, the continuum theory over-predicts the DEM data by less than 35%. This agreement is a substantial improvement to the orders of magnitude spanned by the predictions of past entrainment rate correlations (Chew et al., 2015).

Finally, the presence of agglomerates larger than doublets are a source of discrepancy between the continuum theory and DEM for both agglomerate fraction and entrainment rate. Agglomerates larger than doublets are not accounted for in the continuum theory, but are observed in the DEM simulations, as shown in Fig. 5. A non-monotonic trend is observed in mean agglomerate size. Similar to the behavior for fraction of particles in agglomerates (Fig. 3a and c), two mechanisms compete to cause the non-monotonic trend of mean agglomerate size. First, increased solid volume fraction leads to increased collision frequency and increased agglomeration and breakage. The increase in agglomeration will be greater than the increase in breakage, since large agglomerates form more readily than they break. Second, increased solid volume fraction leads to increased generation of granular energy due to collisions between primary particles and agglomerates. Accordingly, the success factor of breakage increases and the success factor of aggregation decreases, leading to more breakage and less aggregation and smaller agglomerates.

## 4. Conclusions

The recent continuum theory for cohesive particles (Kellogg et al., 2017), which was previously explored in granular systems, was extended to a gas-solid flow in the current work. The agreement between the continuum theory and DEM simulations of the unbounded riser explored here provides support for the validity of the continuum theory for cohesive particles in gas-solid flows. Agglomerate fraction was observed to increase with increasing critical velocity (cohesion), as expected. The continuum theory over-predicts the agglomerate fraction observed in DEM by less than 15% for these cases. As solid volume fraction was increased, a non-monotonic trend of agglomerate fraction was observed. The non-monotonic trend was traced to two competing mechanisms. First, increasing solid volume fraction increases the granular temperature (impact velocity between colliding particles), which causes a decrease of the fraction of particles in agglomerates. Next, at higher solid volume fractions, larger agglomerates form that are harder to break than smaller agglomerates, thereby increasing the fraction of particles in agglomerates. For these cases, the continuum theory generally under-predicts the agglomerate fraction by less than 75% for the cases that were stable in the both the continuum and DEM simulations.

For the cases where the critical velocity was varied, the continuum theory shows a decrease of entrainment rate with increasing critical velocity, while the DEM simulations show a relatively constant entrainment rate. The entrainment rate remains constant since the drag reduction (and corresponding decrease in entrainment rate) due to agglomeration in DEM was less than that in the continuum theory predictions, since agglomerates were treated differently in the drag laws of each method (i.e., discrete vs. continuum). The continuum theory over-predicts the DEM entrainment rate within 15%.

For the cases where the solid volume fraction was varied, the entrainment rate increases nearly linearly as solid volume fraction increases in both the continuum theory predictions and DEM simulations. This nearly linear relationship happens since at the solid volume fractions explored here ($\varepsilon_s$ = 0.0025–0.04), the solids velocity depends weakly on solid volume fraction. The predictions for the entrainment rate are much closer (<35% difference) than differences found among existing correlations (orders-of-magnitude differences). At the lowest solid volume fractions explored ($\varepsilon_s$ = 0.0025–0.005), instabilities are observed in the continuum theory. These instabilities lead to an increase in granular temperature that is not observed in the (stable) DEM simulations, and hence a poor prediction of the entrainment rate and agglomerate fraction from the continuum theory.

One final source of error that should be noted is that the continuum theory only considers singlets and doublets, whereas larger agglomerates are observed to form in the DEM simulations. This affects the accuracy of the predictions of both the entrainment rate and agglomerate fraction.

Future work should include moderately-cohesive particles that form larger agglomerates, and for those larger agglomerates to be included in the continuum theory. Additionally, systems with walls and consequently gradients in the mean flow variables should be considered. The continuum theory has not yet been applied to systems with such gradients, and consequently various terms in the theory (e.g. diffusion of granular energy) have not been tested. Finally, the validity of continuum theory should be validated via comparison with experimental flows.

## Conflict of interest

The authors declare that they have no known competing financial interests or personal relationships that could have appeared to influence the work reported in this paper.

## Acknowledgements

The authors are grateful for the financial support provided by the Dow Corning Corporation, a wholly owned subsidiary of the Dow Chemical Company, and the National Science Foundation (CBET-1707046). The authors thank Casey LaMarche for stimulating discussions. This work utilized the RMACC Summit supercom-

puter, which is supported by the National Science Foundation (Awards ACI-1532235 and ACI-1532236), the University of Colorado Boulder, and Colorado State University. The Summit supercomputer is a joint effort of the University of Colorado Boulder and Colorado State University.

## Appendix A. . Drag closures from extension (Hill et al., 2001) of Koch-Hill-Ladd (Benyahia et al., 2006).

$$K_{g,i} = \frac{3Fd_i^2\rho_g(1-\varepsilon_s)^2|\mathbf{u_g}-\mathbf{u_i}|}{2Re}$$

$$F = \begin{cases} 1+\frac{3}{8}Re, & \varepsilon_s \leqslant 0.01, \quad Re \leqslant \frac{F_2-1}{\frac{3}{8}-F_3} \\ F_0+F_1Re^2, & \varepsilon_s > 0.01, \quad Re \leqslant \frac{F_3+\sqrt{F_3^2-4F_1(F_0-F_2)}}{2F_1} \\ F = F_2+F_3Re, & \varepsilon_s \leqslant 0.01, \quad Re > \frac{F_2-1}{\frac{3}{8}-F_3} \\ F = F_2+F_3Re, & \varepsilon_s > 0.01, \quad Re > \frac{F_3+\sqrt{F_3^2-4F_1(F_0-F_2)}}{2F_1} \end{cases}$$

$$F_0 = \begin{cases} (1-w)\left[\frac{1+3\sqrt{\varepsilon_s/2}+\frac{135}{64}\varepsilon_s\ln(\varepsilon_s)+17.14\varepsilon_s}{1+0.681\varepsilon_s-8.48\varepsilon_s^2+8.16\varepsilon^3}\right]+w\left[\frac{10\varepsilon_s}{(1-\varepsilon_s)^3}\right] & 0.01<\varepsilon_s<0.4 \\ \frac{10\varepsilon_s}{(1-\varepsilon_s)^3} & \varepsilon_s \geqslant 0.4 \end{cases}$$

$$F_1 = \begin{cases} \frac{\sqrt{\frac{\varepsilon_s}{2}}}{40} & 0.01<\varepsilon_s \leqslant 0.1 \\ 0.11+0.00051\exp(11.6\varepsilon_s) & \varepsilon_s > 0.1 \end{cases}$$

$$F_2 = \begin{cases} (1-w)\left[\frac{1+3\sqrt{\varepsilon_s/2}+\frac{135}{64}\varepsilon_s\ln(\varepsilon_s)+17.14\varepsilon_s}{1+0.681\varepsilon_s-11.03\varepsilon_s^2+15.41\varepsilon^3}\right]+w\left[\frac{10\varepsilon_s}{(1-\varepsilon_s)^3}\right] & 0.\varepsilon_s<0.4 \\ \frac{10\varepsilon_s}{(1-\varepsilon_s)^3} & \varepsilon_s \geqslant 0.4 \end{cases}$$

$$F_1 = \begin{cases} 0.9351\varepsilon_s+0.03667 & \varepsilon_s<0.0953 \\ 0.0673+0.212\varepsilon_s+\frac{0.0232}{(1-\varepsilon_s)^5} & \varepsilon_s \geqslant 0.0953 \end{cases}$$

$$w = e^{-10(0.4-\varepsilon_s)/\varepsilon_s}$$

$$Re = \frac{\rho_g(1-\varepsilon_s)|\mathbf{u_g}-\mathbf{u_i}|d_i}{2\mu_g}$$

## References


Anand, A., Curtis, J.S., Wassgren, C.R., Hancock, B.C., Ketterhagen, W.R., 2009. Predicting discharge dynamics of wet cohesive particles from a rectangular hopper using the discrete element method (DEM). Chem. Eng. Sci. 64, 5268–5275.

Benyahia, S., Syamlal, M., O'Brien, T.J., 2006. Extension of Hill–Koch–Ladd drag correlation over all ranges of Reynolds number and solids volume fraction. Powder Technol. 162, 166–174.

Cahyadi, A., Neumayer, A.H., Hrenya, C.M., Cocco, R.A., Chew, J.W., 2015. Comparative study of Transport Disengaging Height (TDH) correlations in gas–solid fluidization. Powder Technol. 275, 220–238.

Castellanos, A., 2005. The relationship between attractive interparticle forces and bulk behaviour in dry and uncharged fine powders. Adv. Phys. 54, 263–376.

Chaudhuri, B., Mehrotra, A., Muzzio, F.J., Tomassone, M.S., 2006. Cohesive effects in powder mixing in a tumbling blender. Powder Technol. 165, 105–114.

Chew, J.W., Cahyadi, A., Hrenya, C.M., Karri, R., Cocco, R.A., 2015. Review of entrainment correlations in gas–solid fluidization. Chem. Eng. J. 260, 152–171.

Figueroa, I., Li, H., McCarthy, J., 2009. Predicting the impact of adhesive forces on particle mixing and segregation. Powder Technol. 195, 203–212.

Galvin, J.E., Benyahia, S., 2014. The effect of cohesive forces on the fluidization of aeratable powders. AIChE J. 60, 473–484.

Garzó, V., Dufty, J.W., 1999. Dense fluid transport for inelastic hard spheres. Phys. Rev. E 59, 5895–5911.

Geldart, D., Harnby, W., Wong, A.C., 1984. Fluidization of cohesive powders. Powder Technol. 37, 25–37.

Gidaspow, D., 1994. Multiphase Flow and Fluidization: Continuum and Kinetic Theory Descriptions. Academic Press, San Diego.

Hill, R.J., Koch, D.L., Ladd, A.J.C., 2001. Moderate-Reynolds-number flows in ordered and random arrays of spheres. J. Fluid Mech. 448.

Hou, Q.F., Zhou, Z.Y., Yu, A.B., 2012. Micromechanical modeling and analysis of different flow regimes in gas fluidization. Chem. Eng. Sci. 84, 449–468.

Iddir, H., Arastoopour, H., 2005. Modeling of multitype particle flow using the kinetic theory approach. AIChE J. 51, 1620–1632.

Kellogg, K.M., Liu, P., LaMarche, C.Q., Hrenya, C.M., 2017. Continuum theory for rapid cohesive-particle flows: general balance equations and discrete-element-method-based closure of cohesion-specific quantities. J. Fluid Mech. 832, 345–382.

Liu, D., van Wachem, B.G.M., Mudde, R.F., Chen, X., van Ommen, J.R., 2016a. An adhesive CFD-DEM model for simulating nanoparticle agglomerate fluidization. AIChE J. 62, 2259–2270.

Liu, P., Kellogg, K.M., LaMarche, C.Q., Hrenya, C.M., 2017. Dynamics of singlet-doublet collisions of cohesive particles. Chem. Eng. J. 324, 380–391.

Liu, P., LaMarche, C.Q., Kellogg, K.M., Leadley, S., Hrenya, C.M., 2016b. Cohesive grains: bridging microlevel measurements to macrolevel flow behavior via surface roughness. AIChE J. 62, 3529–3537.

Liu, P.Y., LaMarche, C.Q., Kellogg, K.M., Hrenya, C.M., 2016c. Fine-particle defluidization: interaction between cohesion, Young's modulus and static bed height. Chem. Eng. Sci. 145, 266–278.

Mansoori, G.A., 1971. Equilibrium thermodynamic properties of the mixture of hard spheres. J. Chem. Phys. 54, 1523.

Mikami, T., Kamiya, H., Horio, M., 1998. Numerical simulation of cohesive powder behavior in a fluidized bed. Chem. Eng. Sci. 53, 1927–1940.

Motlagh, A.H.A., Grace, J.R., Salcudean, M., Hrenya, C.M., 2014. New structure-based model for Eulerian simulation of hydrodynamics in gas–solid fluidized beds of Geldart group "A" particles. Chem. Eng. Sci. 120, 22–36.

Rabinovich, Y.I., Adler, J.J., Ata, A., Singh, R.K., Moudgil, B.M., 2000. Adhesion between nanoscale rough surfaces. J. Colloid Interface Sci. 232, 10–16.

Ringl, C., Bringa, E.M., Bertoldi, D.S., Urbassek, H.M., 2012. Collisions of porous clusters: a granular-mechanics study of compaction and fragmentation. Astrophys. J. 752, 151.

Syamlal, M., Rogers, W., O'Brien, T.J., 1993. MFIX Documentation Theory Guide. National Energy Technology Laboratory, Department of Energy.

van der Hoef, M.A., van Sint Annaland, M., Deen, N.G., Kuipers, J.A.M., 2008. Numerical simulation of dense gas-solid fluidized beds: a multiscale modeling strategy. Annu. Rev. Fluid Mech. 40, 47–70.